

## Article

# Synthesis of MoS<sub>2</sub> Using Chemical Vapor Deposition and Conventional Hydrothermal Methods: Applications to Respiration Sensing

Eunjin Kim <sup>1</sup>, Ja-Yeon Kim <sup>2</sup> and Min-Ki Kwon <sup>1,\*</sup> <sup>1</sup> Department of Photonic Engineering, Chosun University, Gwangju 61452, Republic of Korea<sup>2</sup> Korea Photonics Technology Institute, Gwangju 61452, Republic of Korea

\* Correspondence: mkkwon@chosun.ac.kr; Tel.: +82-62-230-7549

**Abstract:** A promising alternative to methods for the conventional medical diagnosis of many disorders is respiratory monitoring. Unfortunately, current respiratory monitoring methods can be expensive and require inconvenient equipment, significantly limiting their medical applicability. In this study, we fabricated a respiration sensor that uses MoS<sub>2</sub>-based resistance measurements and analyzed the cause of the slow response time previously reported for MoS<sub>2</sub>-based sensors. Our results confirm that the crystal phase change of MoS<sub>2</sub> affects the absorption and desorption of H<sub>2</sub>O and the use of the 2H structure results in high sensitivity, a fast response time, and a linear response to water vapor absorption during breathing. This study demonstrates the potential of two-dimensional nanomaterials for humidity and respiration sensors that can be applied in various fields.

**Keywords:** two-dimensional materials; molybdenum disulfide; respiration sensor; hydrothermal; chemical vapor deposition; MoS<sub>2</sub>



**Citation:** Kim, E.; Kim, J.-Y.; Kwon, M.-K. Synthesis of MoS<sub>2</sub> Using Chemical Vapor Deposition and Conventional Hydrothermal Methods: Applications to Respiration Sensing. *Appl. Sci.* **2023**, *13*, 6084. <https://doi.org/10.3390/app13106084>

Academic Editors: Filippo Giannazzo and Ivan Shteplyuk

Received: 11 April 2023

Revised: 10 May 2023

Accepted: 11 May 2023

Published: 15 May 2023



**Copyright:** © 2023 by the authors. Licensee MDPI, Basel, Switzerland. This article is an open access article distributed under the terms and conditions of the Creative Commons Attribution (CC BY) license (<https://creativecommons.org/licenses/by/4.0/>).

## 1. Introduction

Respiration, the process of gas exchange between an organism and the environment, is critical for sustaining human life and activity [1]. Shortness of breath is a form of discomfort caused by breathing difficulties. Respiratory disorders exhibit various symptoms depending on their cause. Asthma, heart conditions such as heart failure, pneumonia, bronchitis, sleep apnea, fever due to infection, and various other diseases and health conditions can cause respiratory disorders [2]. When experiencing shortness of breath, a feeling of air depletion accompanies an increase in the breathing rate, making alterations in the depth of breathing possible. Breathing causes changes in humidity depending on inhalation and exhalation. Therefore, humidity detection is becoming an increasingly important method of respiratory monitoring, as it offers a promising approach to establish a relationship between human breathing and electrical signals [3]. In addition to work, health and safety, and the analysis of human emotions, respiratory monitoring has also found applications in sports performance and training. The monitoring of breathing during exercise can provide valuable information on the efficiency of breathing patterns and the intensity of exercise. This can help athletes and coaches to optimize training programs and improve performance. For example, tracking respiratory rates during high-intensity interval training can help athletes to determine their optimal rest periods between exercise to maximize the effectiveness of the workout.

Furthermore, respiratory monitoring has been used in the diagnosis and management of various medical conditions and problems. For example, in sleep therapy, respiratory monitoring is used to diagnose and treat sleep apnea, a condition in which a person's breathing repeatedly stops and starts during sleep. In cardiology, respiratory monitoring can provide information on heart function and help to diagnose heart conditions. In addition, respiratory monitoring can also be used to monitor the effects of medications on

respiratory function and to assess the progression of respiratory diseases, such as chronic obstructive pulmonary disease and asthma.

However, to measure 20–30 breaths per minute, a fast response time is required. Nonetheless, the existing humidity sensors have limitations, such as their large size, low sensitivity, sensitivity to temperature changes, and slow response times, which limit their application fields [4]. Through the studies on microelectromechanical systems (MEMS) over the past few decades, miniature humidity sensors have been developed using several different principles, such as capacitance, resistance, resonance, piezoelectric, and optical sensors [1,2,5–8].

Methods for measuring the moisture generated from direct respiration are divided into two types, depending on the measurement technology used: capacitive and resistive electronic humidity sensors.

Capacitive humidity sensors are widely used because of advantages related to their temperature stability, low power consumption, excellent linearity, and wide range of relative humidity measurements [9]. However, their structure is complex, and the management of the capacitance values is challenging, making the manufacturing process complicated and resulting in high numbers of errors due to small changes, which remains an issue to be resolved [10]. Resistive humidity sensors enable precise measurements and are easy to manufacture at low costs. They are also small in size with high degrees of freedom and are suitable for sensor arrays. Owing to these advantages, research is being conducted to replace capacitive humidity sensors with resistive humidity sensors [11–13].

Indeed, many issues remain to be addressed in regard to the resistance-type humidity sensors that have been studied for metal oxides and polymers. These issues include a low response rate, low reactivity in low-humidity environments, hysteresis, and susceptibility to external environmental factors. For example, metal-oxide-based humidity sensors have been shown to degrade significantly in high-temperature and high-humidity environments [14]. Polymer-based humidity sensors exhibit reduced durability in high-humidity environments [15]. Therefore, research on reliable detection materials is necessary to address these issues.

Two-dimensional (2D) materials, such as molybdenum disulfide ( $\text{MoS}_2$ ), with a high surface-to-volume ratio, large specific areas, and numerous active sites, such as graphene and transition metal dichalcogenides (TMD), have demonstrated considerable potential as sensing materials [13,16–18]. In general, 2D TMDs belong to a family of layered semi-conducting structures with the chemical formula of  $\text{MX}_2$ , where M represents a transition metal atom such as Mo or W, and X is a chalcogen atom such as Se or S. The layered nature of these materials results in strong anisotropy in their physical and chemical properties, such as their electrical, mechanical, and thermal properties. The most extensively studied 2D-TMD is  $\text{MoS}_2$ , which has three crystalline structures: 1T (tetragonal), 2H (hexagonal), and 3R (rhombohedral) [19]. The lattice parameters of 1T  $\text{MoS}_2$  are 5.6 Å and 5.99 Å, those of 2H  $\text{MoS}_2$  are 3.15 Å and 12.36 Å, and those of 3R  $\text{MoS}_2$  are 3.17 Å and 18.38 Å [20]. Furthermore, the electronic properties of  $\text{MoS}_2$  vary with the phase; it behaves as a metal in the 1T phase and as a semiconductor in the 2H and 3R phases [19,20]. Among the mono- to few-layer structures, 2H- $\text{MoS}_2$  is the most thermodynamically stable and commonly found phase. In its monolayer form,  $\text{MoS}_2$  has an octahedral or a trigonal prismatic coordination phase [21].

However, the progress made in humidity-sensing technology based on pure  $\text{MoS}_2$  is not substantial. These sensors have exhibited low reactivity at low humidity levels and even longer recovery times of over 30 s, showing even lower recovery rates than the existing capacitive humidity sensors. Further studies are required to identify and address the causes of these issues [22,23].

X. Gan reported that the crystal phase of  $\text{MoS}_2$ , having S vacancies, reduced the bandgap of  $\text{MoS}_2$ , indicating an increased conductivity and decrease in the hydrogen adsorption free energy, implying a significant improvement of hydrogen evolution reaction activity [24]. J. Cao reported that there is a significant change in the density of states near

the Fermi level as well as greater charge transfer between the gas and the MoS<sub>2</sub> when the gas is adsorbed onto 1T' MoS<sub>2</sub> and WS<sub>2</sub> compared to 2H MoS<sub>2</sub> and WS<sub>2</sub>. Thus, phase selection is important for improving the gas-sensing performance of monolayer MoS<sub>2</sub> and WS<sub>2</sub> [25]. However, the crystalline nature of MoS<sub>2</sub> in response to respiration has not been studied.

In this study, we attempted to determine the origin of the slow recovery rates of MoS<sub>2</sub>-based respiration sensors. We compared two respiration sensors fabricated using MoS<sub>2</sub> synthesized using the chemical vapor deposition (CVD) and hydrothermal methods.

We confirmed that the crystallinity of MoS<sub>2</sub> thin films varies greatly depending on the synthesis method. It was confirmed that the change in the crystal structure greatly affects the adsorption and desorption of water vapor. In this research, we confirmed that the problem with MoS<sub>2</sub> humidity sensors and respiration sensors, which made it difficult to secure a fast response speed, was caused by the crystal structure.

## 2. Experimental

### 2.1. Synthesis of MoS<sub>2</sub> by Hydrothermal Method

Figure 1 shows a schematic of the synthesis of MoS<sub>2</sub> grown via thermal synthesis and CVD. For the synthesis of MoS<sub>2</sub> samples via the hydrothermal method, Na<sub>2</sub>MoO<sub>4</sub>·2H<sub>2</sub>O (0.15 g) and CH<sub>3</sub>CSNH<sub>2</sub> (0.6 g) were dissolved in 50 mL of deionized (DI) water, and the obtained MoS<sub>2</sub> was heated for 24 h at 200 °C in an autoclave. The resultant MoS<sub>2</sub> was centrifuged and the remaining solution was discarded. Then, MoS<sub>2</sub> was mixed with DI water for drop casting. To separate the micro-sized MoS<sub>2</sub>, the mixed solution was dispersed using a homogenizer, and a certain amount of MoS<sub>2</sub> was coated onto the sample using the drop-casting method. Then, the MoS<sub>2</sub> was dried for 10 min at 80 °C.

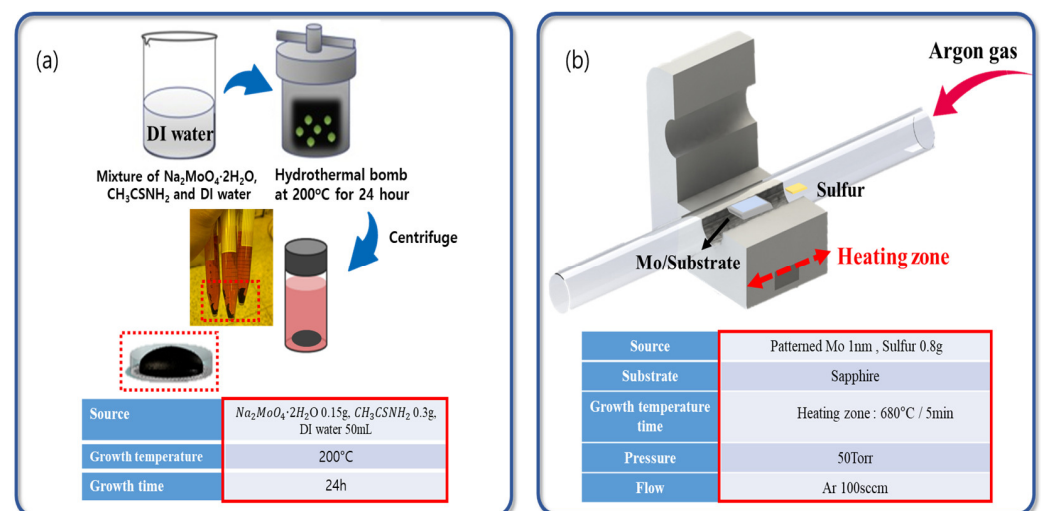


**Figure 1.** Schematic of the synthesis of MoS<sub>2</sub> through the (a) hydrothermal method and (b) CVD method.

### 2.2. Synthesis of MoS<sub>2</sub> via CVD

For the synthesis of MoS<sub>2</sub> samples via CVD, the following process was used: For the deposition of the 0.8 nm thick Mo film, c-plane (0001) sapphires were cleaned in acetone, methanol, deionized (DI) wafer, and buffer oxide etch (BOE). Then, the c-plane (0001) sapphires were rinsed with DI water and blown until dry with N<sub>2</sub> gas. After the lithographic patterning of the photoresist layer with square windows (500 μm<sup>2</sup>) using photolithography, a 0.8 nm thin film of Mo was deposited on a c-plane (0001) sapphire substrate via e-beam evaporation. Next, the patterned Mo thin films deposited on the sapphire substrates were placed in a quartz boat, which, in turn, was placed in the center of a tube furnace. A ceramic boat holding pure sulfur (>99.99%, 0.8 g, Sigma-Aldrich) was placed in the upwind low-temperature zone in the quartz tube. The quartz tube was first

kept under a flow of high-purity Ar at a flow rate of 100 sccm. The growth temperature was 750 °C. The temperature was increased from room temperature to the growth temperature over 10 min and maintained for 5 min before being cooled to room temperature for 60 min.

### 2.3. Fabrication of a Respiration Sensor

To fabricate high-quality, large-area MoS<sub>2</sub> for use as a humidity and respiration sensor, a TFT (thin film transistor) structure was used as the channel for the electron flow, as shown in Figure 2. For the samples synthesized using the hydrothermal method, Ti/Au (5 nm/50 nm) was deposited on a PI substrate using an e-beam evaporation system with a shadow mask. The MoS<sub>2</sub> solution was then dropped onto the channel region between the two electrodes and dried.

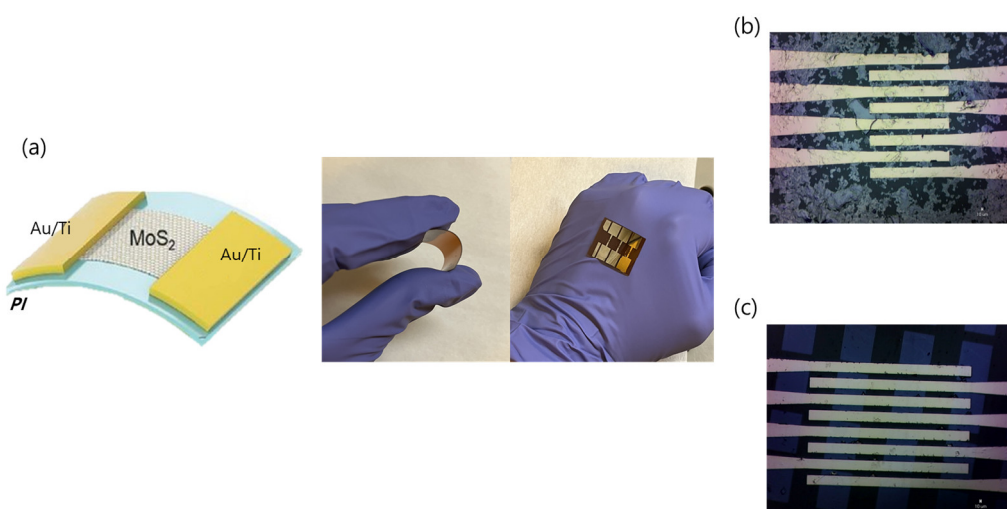


**Figure 2.** Schematic of the synthesis of a respiration sensor: schematic diagram of (a) MoS<sub>2</sub>; MoS<sub>2</sub> synthesized using the (b) hydrothermal method and (c) CVD method.

To fabricate a respiration sensor using the MoS<sub>2</sub> film synthesized via CVD, the MoS<sub>2</sub> film was transferred onto a PI substrate using a wet transfer technique. Poly(methyl methacrylate) (PMMA) was spin-coated onto the MoS<sub>2</sub>/sapphire at 3000 rpm for 60 s. The PMMA/MoS<sub>2</sub> film was immersed in a BOE solution. The solution penetrated the interface between the MoS<sub>2</sub> and sapphire and caused the sapphire substrate to sink. Consequently, the sapphire was separated from MoS<sub>2</sub>/PMMA film and the film remained on the surface of the BOE solution. The PMMA/MoS<sub>2</sub> film was rinsed with DI water for 10 min to remove any effects of the BOE solution. The film was then transferred onto a PI substrate and dried completely at room temperature to ensure adhesion between the MoS<sub>2</sub> film and substrate. The PMMA film was dissolved in acetone and the residue was removed through annealing in Ar at 150 °C for 30 min.

### 2.4. Measurement of Material Characterization

To analyze the optical properties, micro-Raman scattering spectroscopy (RSS) was performed on the dimple-etched sample surfaces using a 532 nm laser with a power density of 0.75 W/m<sup>2</sup> (a 100 μm<sup>2</sup> beam size and a 0.75 μW laser intensity) using a spectrometer (XPER RAM C, Nanobase). An optical microscope (BX-43, Olympus) and scanning electron microscope (SNE-4500M, SEC) were utilized to characterize the surface morphology of the MoS<sub>2</sub> synthesized using the hydrothermal method and CVD. The chemical bonding states of the MoS<sub>2</sub> thin layers and their phase evolution after sulfurization were revealed via X-ray photoelectron spectroscopy (XPS) measurements (K-Alpha+, Thermo Fisher Scientific). A 400 μm diameter X-ray beam operating at 6 mA × 12 kV was utilized to acquire spectra in the constant analyzer energy mode with a pass energy of 200 eV for the survey. Narrow regions were collected using the snapshot acquisition mode (150 eV pass energy) with a

rapid collection rate of 5 s per region. Charge compensation was accomplished using the flood gun system, which supplied low-energy electrons and low-energy argon ions (20 eV) from a single source. Data acquisition and processing were performed using Thermo Scientific Avantage software. Spectral calibration was conducted using an automated calibration routine and the internal standards of Au, Ag, and Cu.

### 2.5. Measurement of Characterization of Respiration Sensor

Prior to the measurement of the respiration sensor, the current response to changes in humidity was measured. For this purpose, TR-72WB, a commercially available capacitance-type moisture sensor, was used, and its current response was measured while rapidly changing the relative humidity from 40 to 60%. A Keithley 4200A-SCS Parameter Analyzer was used to measure the current response. To measure the respiration sensor, the sensor was attached to the front of the face mask, and the reactivity was measured according to the distance or speed of change in the amount of water vapor during respiration. Since respiration-induced changes in moisture content usually occur in the 40–70% interval, we confirmed the current response to moisture in this range. After attaching the sensor to the front of the face mask, it was fixed using tongs, and the current response was analyzed by connecting the sensor to the parameter analyzer.

## 3. Results and Discussion

First, the responses of the TFT-based humidity sensors fabricated using the MoS<sub>2</sub> thin film synthesized via the hydrothermal and CVD synthesis methods were compared. For comparison, the humidity in the range of approximately 40–60% was measured using a commercial capacitance-type sensor (TR-72WB). Because a capacitor-type sensor was used as a reference to measure the humidity variation, it was difficult to change the humidity quickly.

As shown in Figure 3, the currents in both sensors increased with increasing humidity. Generally, when water vapors are adsorbed, superoxides (O<sup>2-</sup>) dominate the dissociation of water molecules at room temperature. The resulting OH<sup>-</sup> is chemically adsorbed onto MoS<sub>2</sub>, serving as an electron donor and increasing the conductivity of the n-type MoS<sub>2</sub> semiconductor, leading to an increase in the current [26,27]. The sensor using hydrothermally synthesized MoS<sub>2</sub> exhibited a fast response to water vapor absorption but a slow recovery time, as shown in Figure 3a. Although the fabricated sensor showed a relatively faster recovery rate compared to the commercial sensor, it was not able to achieve a sufficiently high recovery rate to observe breathing. Similar results have been reported previously [23]. To evaluate the applicability of MoS<sub>2</sub> as a respiration sensor, it is essential to determine whether the problem lies in the moisture absorption of the MoS<sub>2</sub> film itself or if there are other external factors at work.

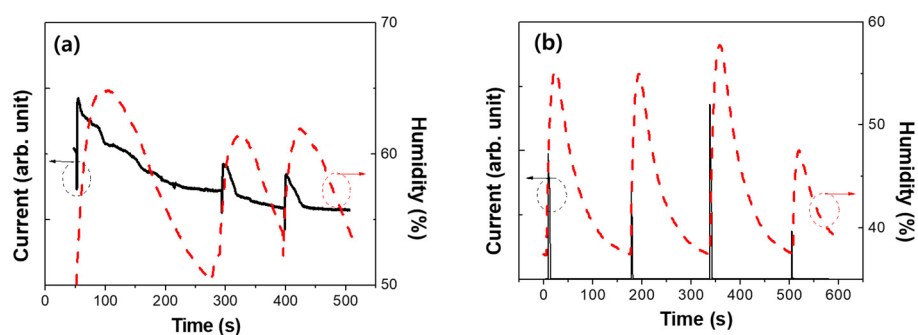
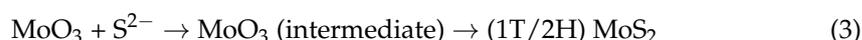
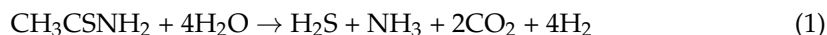


**Figure 3.** Current response depending on the humidity change for samples synthesized via (a) the hydrothermal method and (b) CVD.

The current response of the humidity sensor fabricated using MoS<sub>2</sub> synthesized via CVD, as compared to that fabricated with hydrothermally synthesized MoS<sub>2</sub>, increased as the humidity increased from 40% to 55%. As shown in Figure 3b, the sensor fabricated

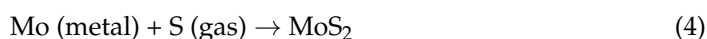
using MoS<sub>2</sub> synthesized via CVD exhibited much faster response and recovery rates than the conventional sensor fabricated using hydrothermally synthesized MoS<sub>2</sub>. This indicates that the fabricated sensor was highly sensitive to changes in humidity. However, these results differ from those of previously reported studies on sensors with a slow recovery time [23]. Therefore, the differences in the response and recovery rates between humidity sensors fabricated using MoS<sub>2</sub> synthesized via CVD and those fabricated hydrothermal method were examined.

In the hydrothermal method, the mechanism underlying the formation of MoS<sub>2</sub> is associated with the anion exchange and reduction reactions described by the following equations [28]:



At first, CH<sub>3</sub>CSNH<sub>2</sub> is decomposed to produce S<sup>2-</sup> anions through the hydrolyzation steps. Then, MoS<sub>2</sub> (intermediate) is formed through a direct anion exchange reaction between the O<sup>2-</sup> anion of MoO<sub>3</sub> and S<sup>2-</sup> anions of sulfur. Finally, MoS<sub>3</sub> is reduced to the 1T and 2H phases of MoS<sub>2</sub> as the final product.

In the CVD method, the mechanism underlying the formation of MoS<sub>2</sub> can be described by the following equations [29]:



The growth of the continuous MoS<sub>2</sub> thin films includes three major steps:

- (1) The reaction of Mo and S to form the MoS<sub>2</sub> nuclei on the surface;
- (2) MoS<sub>2</sub> growth on the substrate, which is controlled by kinetic factors (e.g., temperature, pressure, and the growth time);
- (3) The coalescence of adjacent MoS<sub>2</sub> domains that merge into a continuous film.

In general, since CVD is synthesized at a high temperature of 500 degrees or more, it is common to obtain a 2H crystal structure.

Thus, we believe that there are differences in the crystal phase of MoS<sub>2</sub> depending on the synthesis method. We attempted to analyze the differences in the crystal phase and their effect on the humidity response. First, we analyzed the crystal characteristics of films grown using different growth methods. Figure 4a,b shows the optical microscopy and SEM images of the hydrothermally synthesized MoS<sub>2</sub>. As shown in Figure 4, the hydrothermally synthesized MoS<sub>2</sub> formed a thin film with micro-sized particles dispersed in a plane. In contrast, the optical microscopy (Figure 4d) and SEM images (Figure 4e) of the MoS<sub>2</sub> synthesized via CVD show that the MoS<sub>2</sub> grew well into a thin, nanometer-thick film in the patterned area. Although the shapes of the MoS<sub>2</sub> synthesized via the two methods were different, Raman analysis confirmed that the MoS<sub>2</sub> thin film was well-formed. As shown in Figure 4c,f, E<sup>1</sup><sub>2g</sub> and A<sub>1g</sub>, which are the characteristic peaks of MoS<sub>2</sub>, occurred in both samples. This shows that the MoS<sub>2</sub> thin films were well-formed using both synthesis methods. The E<sup>1</sup><sub>2g</sub> mode is the horizontal vibration peak of Mo and S, whereas the A<sub>1g</sub> mode is the vertical vibration peak of sulfur. As the thickness increased, the E<sup>1</sup><sub>2g</sub> peak shifted to a lower frequency because of the van der Waals forces between the layers, which caused the vibration direction to be perpendicular to the bonding force, whereas the A<sub>1g</sub> peak shifted to a higher frequency because the vibration direction was consistent with the bonding force. The layer number of MoS<sub>2</sub> can be predicted from the interval between the E<sup>1</sup><sub>2g</sub> and A<sub>1g</sub> peaks. A narrow peak interval indicates single-layer MoS<sub>2</sub>, which shows a peak interval of approximately 21 cm<sup>-1</sup>. A wider peak interval indicates bulk MoS<sub>2</sub>. As shown in Figure 4, Raman analysis of the MoS<sub>2</sub> grown via the sequential synthesis and CVD methods showed that the MoS<sub>2</sub> grown using the hydrothermal method had an E<sup>1</sup><sub>2g</sub>

mode of approximately  $382.1\text{ cm}^{-1}$  and an  $A_{1g}$  mode of approximately  $408.3\text{ cm}^{-1}$ , with a peak interval of approximately  $26\text{ cm}^{-1}$ , indicating that the  $\text{MoS}_2$  grew with a thickness of three or more layers. In contrast, the Raman analysis results of the  $\text{MoS}_2$  grown using the CVD method showed an  $E^{1}_{2g}$  mode at approximately  $384\text{ cm}^{-1}$  and an  $A_{1g}$  mode at approximately  $405\text{ cm}^{-1}$ , with a peak interval of  $21\text{ cm}^{-1}$ , indicating that the  $\text{MoS}_2$  grew with a thickness between that of the monolayer and bilayer. Although variations in the desorption and absorption of water vapor might exist due to differences in thickness, we focused on different points.

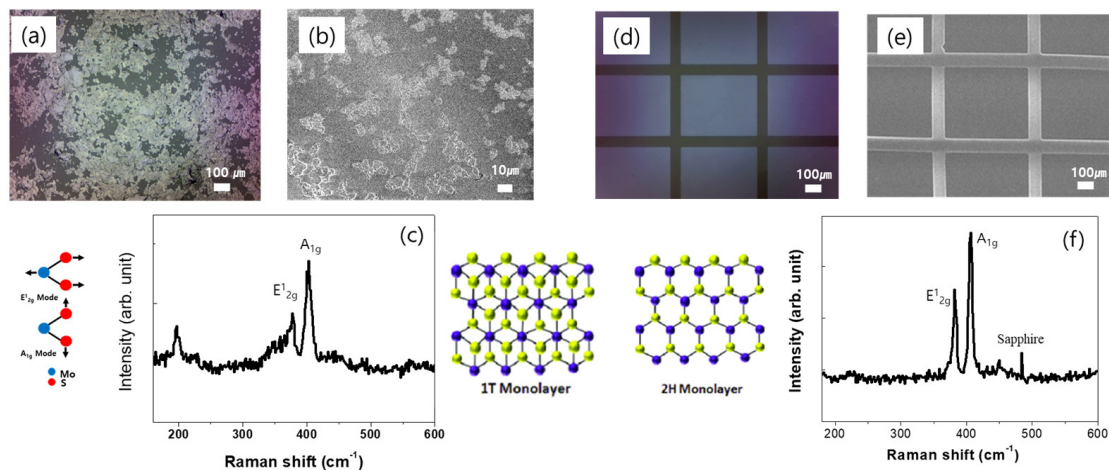


**Figure 4.** (a) Microscopic image, (b) SEM image, and (c) Raman spectrum of  $\text{MoS}_2$  synthesized using the hydrothermal method. (d) Microscopic image, (e) SEM image, and (f) Raman spectrum of  $\text{MoS}_2$  synthesized using the CVD method.

As shown in Figure 4c,f, a unique peak occurred at  $\sim 200\text{ cm}^{-1}$  in the hydrothermally synthesized sample among the  $\text{MoS}_2$  thin films grown using the two growth methods. This change in the Raman peak is due to the structural change in the material itself, and it has a shape that matches that of the 1T-phase molybdenum disulfide [30]. In the hydrothermal method, the 2H structure is destabilized by a second solvent-thermal reaction during sequential synthesis, and to improve the stability, to a certain extent, it is transformed into a 1T structure. Therefore, the optimal structure in which the 2H and 1T phases coexisted is ultimately formed [31]. Consequently, the hydrothermally synthesized  $\text{MoS}_2$  develops a 1T@2H structure, and the CVD-synthesized  $\text{MoS}_2$  develops a 2H structure. Cao reported that the crystal phase is important for the gas-sensing performance [25]. The binding energies of 1T  $\text{MoS}_2$  and 2H  $\text{MoS}_2$  are different, as observed via DFT modeling, which causes the adsorption rate, sensitivity, and desorption rate of the gas to change. Therefore, the improved sensitivity of the humidity sensor fabricated using CVD-synthesized  $\text{MoS}_2$  can be attributed to its 2H crystal phase. In addition, the rate and strength of the adsorption and desorption of water can vary depending on the crystal phase change.

For further verification, XPS (X-ray photoelectron spectroscopy) was used to analyze different phase compositions of  $\text{MoS}_2$ . Figure 5 shows the Mo 3d and S 2p peaks of the XPS spectra of the CVD and hydrothermally synthesized  $\text{MoS}_2$ . For the CVD-synthesized  $\text{MoS}_2$ , two distinct peaks are found at 232.6 eV and 229.4 eV, corresponding to  $3d_{3/2}$  and  $3d_{5/2}$  of  $\text{Mo}^{4+}$ , thus indicating the presence of the 2H phase in  $\text{MoS}_2$ . Additionally, the weak peak at 226.5 eV is the S 2s of  $\text{MoS}_2$ . The new peaks that appear at around 235.5 eV for Mo 3d and 169 eV for S 2p regions can be attributed to the partial oxidation of unsaturated Mo and S atoms in the air. These results indicate that the 2H structure of  $\text{MoS}_2$  was successfully synthesized with the CVD method.

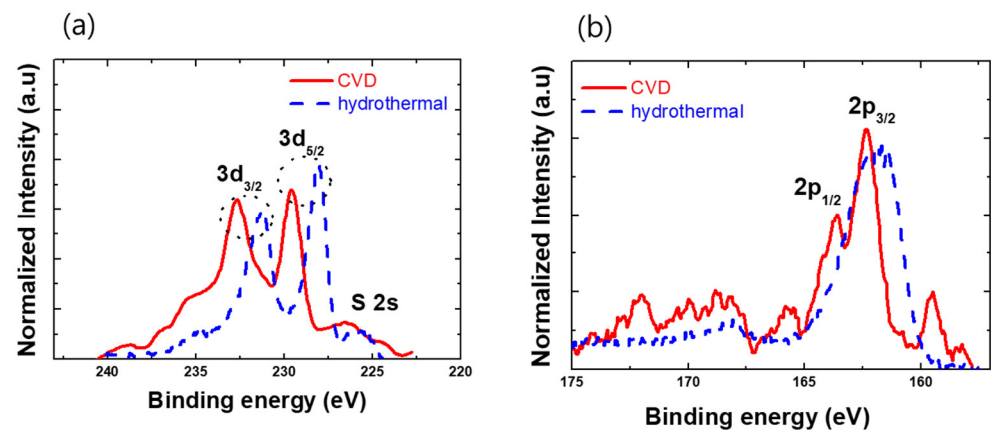


**Figure 5.** High-resolution XPS spectra of the (a) Mo 3d core level and (b) 2p core level of MoS<sub>2</sub> synthesized via the CVD and hydrothermal methods.

As shown in Figure 5a, for the hydrothermally synthesized sample, the 3d<sub>3/2</sub> and 3d<sub>5/2</sub> peaks are shown to be 231.4 and 228.4 eV, respectively. These values are lower than those of the Mo<sup>4+</sup> peak of the 2H MoS<sub>2</sub>. Hydrothermal synthesis generates more S defects than 2H crystal MoS<sub>2</sub>. Additionally, it can be seen that the S 2s peak is lower than the 3d<sub>3/2</sub> and 3d<sub>5/2</sub> peaks. In addition, in the case of the S peak, the S 2P peak also shows that the binding energy of the hydrothermally synthesized MoS<sub>2</sub> is smaller than that of the CVD-synthesized MoS<sub>2</sub>. It can be seen that the half-width value is large for the hydrothermally synthesized MoS<sub>2</sub>. This indirectly indicates that a thin film with many defects, such as S defects, was formed. These defects impede the bonding of Mo and S ions, thus lowering the bonding energy. These results are consistent with the previously reported results. In addition, the results are consistent with the results of the prior to Raman analysis.

The fabrication of a respiratory sensor using MoS<sub>2</sub> grown via the hydrothermal method was challenging owing to the desorption of the synthesized MoS<sub>2</sub> because of the slow response. A respiration sensor using a hydrothermally synthesized MoS<sub>2</sub> thin film has a response time of several tens of seconds, making it impossible to obtain a quick response. Therefore, a respiration sensor was fabricated using only MoS<sub>2</sub> synthesized via CVD. A humidity sensor was installed on the mask, as shown in Figure 6, to measure the response to respiration, and tests were carried out under various conditions. To determine whether the sensor responded sensitively to changes in humidity, the current response was examined as the humidity increased in various humidity environments. For the experiment on the humidity change, the manufactured sensor was loaded into a commercial humidity chamber, and the current was measured while changing the humidity. In order to observe the resistance change of the MoS<sub>2</sub> thin film placed between the two electrodes, the current response was analyzed while the voltage was varied from 0 to 5 V. As the relative humidity increased to 45–75%, the current significantly, linearly increased, indicating that it had the tendency to respond sensitively to changes in the amount of water vapor emitted during respiration. During the respiration analysis, the voltage was set at a constant value of 5 V, while the change in the current over time was observed. To monitor the reactivity of the sensor with respect to the distance between the nose and the sensor, measurements were repeatedly performed at distances of 3, 5, and 10 cm. The current value decreased as the distance increased; however, the respiratory response was maintained. In addition, the responses to each distance exhibited almost identical current changes, demonstrating excellent responsiveness. When measuring normal and rapid breathing, the sensor efficiently followed rapid changes in the breathing rate, and the response and recovery times of the sensor were measured to be approximately 0.4 s. This speed is sufficient to measure the respiration rate of humans.

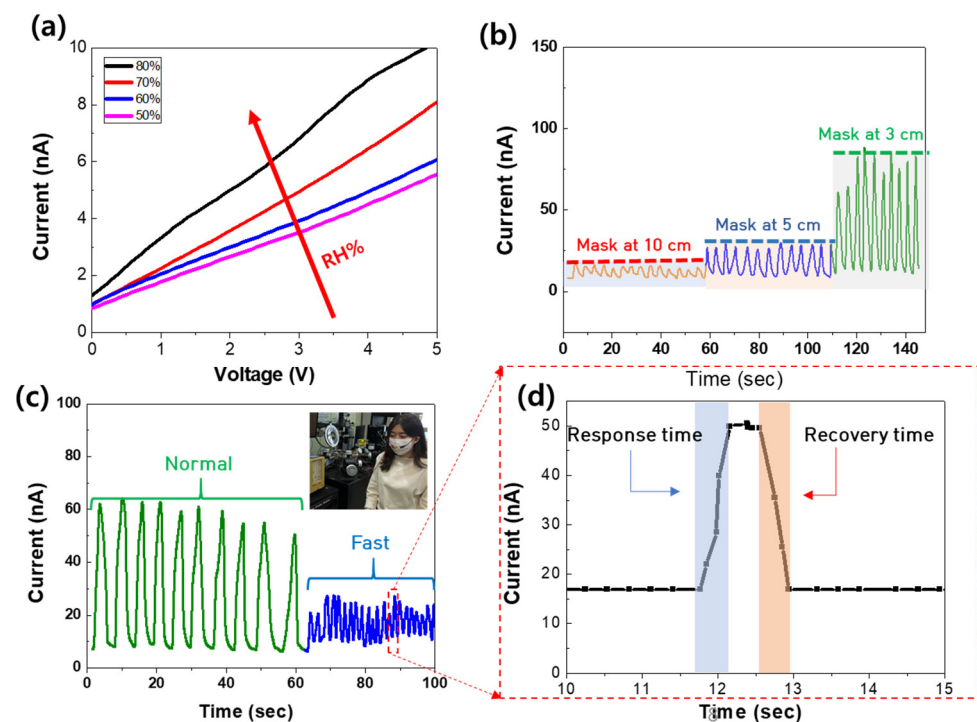


**Figure 6.** (a) Voltage–current curve depending on humidity, (b) current response depending on the distance between the nose and sensor, (c) current response depending on normal and fast breathing, and (d) current response with single breathing.

The results of this study, indeed, confirm that the crystal structure plays a significant role in enhancing the reaction rate for the absorption and desorption of water vapor and respiration reactions. To achieve a more precise analysis, it is necessary to perform DFT modeling specifically focused on the mechanisms of water vapor adsorption and desorption while considering the crystal structure. It is also necessary to analyze the crystallinity, doping, and defects of the MoS<sub>2</sub> thin film. By identifying the exact mechanism through future research, it will become possible to manufacture a MoS<sub>2</sub>-based respiration sensor with an optimal reaction speed.

#### 4. Conclusions

In this study, the cause of the low reactivity of MoS<sub>2</sub>-based respiratory sensors was analyzed based on the crystallinity of MoS<sub>2</sub> according to the synthesis method. The analysis showed that the formation of the 1T@2H structure was a major cause of the slow recovery and that the response and recovery speed improved sufficiently, enabling the sensor to be sensitive to respiratory reactions when high-quality 2H crystal structures were formed using CVD synthesis. These results based on methods that can be utilized as a fundamental technology significantly contribute to efforts for improving human health by preventing major diseases or accidents through the monitoring of abnormal breathing.

**Author Contributions:** M.-K.K. and E.K. conceived and designed the experiments; E.K. performed the experiments; J.-Y.K. and M.-K.K. analyzed the data; and M.-K.K. wrote the manuscript. All authors have read and agreed to the published version of the manuscript.

**Funding:** This study was supported by a research fund from Chosun University, 2022.

**Institutional Review Board Statement:** Not applicable.

**Informed Consent Statement:** Not applicable.

**Data Availability Statement:** All datasets are publicly available.

**Conflicts of Interest:** The authors declare no conflict of interest.

## References

1. Dinh, T.; Nguyen, T.; Phan, H.P.; Nguyen, N.T.; Dao, D.V.; Bell, J. Stretchable respiration sensors: Advanced designs and multifunctional platforms for wearable physiological monitoring. *Biosens. Bioelectron.* **2020**, *166*, 112460. [[CrossRef](#)] [[PubMed](#)]
2. Dai, J.X.; Zhao, H.R.; Lin, X.Z.; Liu, S.; Liu, Y.S.; Liu, X.P.; Fei, T.; Zhang, T. Ultrafast Response Polyelectrolyte Humidity Sensor for Respiration Monitoring. *ACS Appl. Mater. Interface* **2019**, *11*, 6483–6490. [[CrossRef](#)] [[PubMed](#)]
3. Lu, L.J.; Jiang, C.P.; Hu, G.S.; Liu, J.Q.; Yang, B. Flexible Noncontact Sensing for Human-Machine Interaction. *Adv. Mater.* **2021**, *33*, 2100218. [[CrossRef](#)]
4. Zhou, L.J.; Wang, M.Y.; Liu, Z.H.; Guan, J.R.; Li, T.T.; Zhang, D.Z. High-performance humidity sensor based on graphitic carbon nitride/polyethylene oxide and construction of sensor array for non-contact humidity detection. *Sens. Actuators B Chem.* **2021**, *344*, 130219. [[CrossRef](#)]
5. Dai, C.L. A capacitive humidity sensor integrated with micro heater and ring oscillator circuit fabricated by CMOS-MEMS technique. *Sens. Actuators B Chem.* **2007**, *122*, 375–380. [[CrossRef](#)]
6. Iyengar, S.A.; Srikrishnarka, P.; Jana, S.K.; Islam, M.R.; Ahuja, T.; Mohanty, J.S.; Pradeep, T. Surface-Treated Nanofibers as High Current Yielding Breath Humidity Sensors for Wearable Electronics. *ACS Appl. Electron. Mater.* **2019**, *1*, 951–960. [[CrossRef](#)]
7. Jeong, W.; Song, J.; Bae, J.; Nandanapalli, K.R.; Lee, S. Breathable Nanomesh Humidity Sensor for Real-Time Skin Humidity Monitoring. *ACS Appl. Mater. Interface* **2019**, *11*, 44758–44763. [[CrossRef](#)]
8. Le, X.H.; Liu, Y.H.; Peng, L.; Pang, J.T.; Xu, Z.; Gao, C.; Xie, J. Surface acoustic wave humidity sensors based on uniform and thickness controllable graphene oxide thin films formed by surface tension. *Microsyst. Nanoeng.* **2019**, *5*, 36. [[CrossRef](#)]
9. Lazarus, N.; Bedair, S.S.; Lo, C.C.; Fedder, G.K. CMOS-MEMS Capacitive Humidity Sensor. *J. Microelectromech. Syst.* **2010**, *19*, 183–191. [[CrossRef](#)]
10. Lee, J.; Mulmi, S.; Thangadurai, V.; Park, S.S. Magnetically Aligned Iron Oxide/Gold Nanoparticle-Decorated Carbon Nanotube Hybrid Structure as a Humidity Sensor. *ACS Appl. Mater. Interface* **2015**, *7*, 15506–15513. [[CrossRef](#)]
11. Lim, D.I.; Cha, J.R.; Gong, M.S. Preparation of flexible resistive micro-humidity sensors and their humidity-sensing properties. *Sens. Actuators B Chem.* **2013**, *183*, 574–582. [[CrossRef](#)]
12. Smith, A.D.; Elgammal, K.; Niklaus, F.; Delin, A.; Fischer, A.C.; Vaziri, S.; Forsberg, F.; Rasander, M.; Hugosson, H.; Bergqvist, L.; et al. Resistive graphene humidity sensors with rapid and direct electrical readout. *Nanoscale* **2015**, *7*, 19099–19109. [[CrossRef](#)] [[PubMed](#)]
13. Burman, D.; Ghosh, R.; Santra, S.; Guha, P.K. Highly proton conducting MoS<sub>2</sub>/graphene oxide nanocomposite based chemoresistive humidity sensor. *RSC Adv.* **2016**, *6*, S7424–S7433. [[CrossRef](#)]
14. Wang, C.X.; Yin, L.W.; Zhang, L.Y.; Xiang, D.; Gao, R. Metal Oxide Gas Sensors: Sensitivity and Influencing Factors. *Sensors* **2010**, *10*, 2088–2106. [[CrossRef](#)] [[PubMed](#)]
15. Wang, X.F.; Ding, B.; Yu, J.Y.; Wang, M.R. Highly sensitive humidity sensors based on electro-spinning/netting a polyamide 6 nano-fiber/net modified by polyethyleneimine. *J. Mater. Chem.* **2011**, *21*, 16231–16238. [[CrossRef](#)]
16. Zhao, J.; Li, N.; Yu, H.; Wei, Z.; Liao, M.Z.; Chen, P.; Wang, S.P.; Shi, D.X.; Sun, Q.J.; Zhang, G.Y. Highly Sensitive MoS<sub>2</sub> Humidity Sensors Array for Noncontact Sensation. *Adv. Mater.* **2017**, *29*, 1702076. [[CrossRef](#)]
17. Guo, L.F.; Li, X.Y.; Li, W.X.; Gou, C.C.; Zheng, M.F.; Zhang, Y.; Chen, Z.Y.; Hong, Y. High-sensitive humidity sensor based on MoS<sub>2</sub>/graphene oxide quantum dot nanocomposite. *Mater. Chem. Phys.* **2022**, *287*, 126146. [[CrossRef](#)]
18. Pereira, N.M.; Rezende, N.P.; Cunha, T.H.R.; Barboza, A.P.M.; Silva, G.G.; Lippross, D.; Neves, B.R.A.; Chacham, H.; Ferlauto, A.S.; Lacerda, R.G. Aerosol-Printed MoS<sub>2</sub> Ink as a High Sensitivity Humidity Sensor. *ACS Omega* **2022**, *7*, 9388–9396. [[CrossRef](#)]
19. Song, I.; Park, C.; Choi, H.C. Synthesis and properties of molybdenum disulphide: From bulk to atomic layers. *RSC Adv.* **2015**, *5*, 7495–7514. [[CrossRef](#)]
20. Zhao, Z.Y.; Liu, Q.L. Study of the layer-dependent properties of MoS<sub>2</sub> nanosheets with different crystal structures by DFT calculations. *Catal. Sci. Technol.* **2018**, *8*, 1867–1879. [[CrossRef](#)]
21. Kan, M.; Wang, J.Y.; Li, X.W.; Zhang, S.H.; Li, Y.W.; Kawazoe, Y.; Sun, Q.; Jena, P. Structures and Phase Transition of a MoS<sub>2</sub> Monolayer. *J. Phys. Chem. C* **2014**, *118*, 1515–1522. [[CrossRef](#)]
22. Park, S.Y.; Kim, Y.H.; Lee, S.Y.; Sohn, W.; Lee, J.E.; Kim, D.H.; Shim, Y.S.; Kwon, K.C.; Choi, K.S.; Yoo, H.J.; et al. Highly selective and sensitive chemoresistive humidity sensors based on rGO/MoS<sub>2</sub> van der Waals composites. *J. Mater. Chem. A* **2018**, *6*, 5016–5024. [[CrossRef](#)]
23. Awais, M.; Khan, M.U.; Hassan, A.; Bae, J.; Chattha, T.E. Printable Highly Stable and Superfast Humidity Sensor Based on Two Dimensional Molybdenum Diselenide. *Sci. Rep.* **2020**, *10*, 5509. [[CrossRef](#)] [[PubMed](#)]
24. Gan, X.R.; Lee, L.Y.S.; Wong, K.Y.; Lo, T.W.; Ho, K.H.; Lei, D.Y.; Zhao, H.M. 2H/1T Phase Transition of Multilayer MoS<sub>2</sub> by Electrochemical Incorporation of S Vacancies. *ACS Appl. Energy Mater.* **2018**, *1*, 4754–4765. [[CrossRef](#)]
25. Cao, J.M.; Zhou, J.; Chen, J.Y.; Wang, W.Q.; Zhang, Y.F.; Liu, X.W. Effects of Phase Selection on Gas-Sensing Performance of MoS<sub>2</sub> and WS<sub>2</sub> Substrates. *ACS Omega* **2020**, *5*, 28823–28830. [[CrossRef](#)]
26. Ghuman, K.K.; Yadav, S.; Singh, C.V. Adsorption and Dissociation of H<sub>2</sub>O on Monolayered MoS<sub>2</sub> Edges: Energetics and Mechanism from ab Initio Simulations. *J. Phys. Chem. C* **2015**, *119*, 6518–6529. [[CrossRef](#)]
27. Mondal, S.; Kim, S.J.; Choi, C.G. Honeycomb-like MoS<sub>2</sub> Nanotube Array-Based Wearable Sensors for Noninvasive Detection of Human Skin Moisture. *ACS Appl. Mater. Interface* **2020**, *12*, 17029–17038. [[CrossRef](#)]

28. Duraisamy, S.; Ganguly, A.; Sharma, P.K.; Benson, J.; Davis, J.; Papakonstantinou, P. One-Step Hydrothermal Synthesis of Phase-Engineered MoS<sub>2</sub>/MoO<sub>3</sub> Electrocatalysts for Hydrogen Evolution Reaction. *ACS Appl. Nano Mater.* **2021**, *4*, 12. [[CrossRef](#)]
29. Kim, M.W.; Kim, J.Y.; Cho, Y.H.; Park, H.S.; Kwon, M.K. Role of the Growth Temperature in MoS<sub>2</sub> Growth by Chemical Vapor Deposition. *J. Nanosci. Nanotechnol.* **2018**, *18*, 2140–2143. [[CrossRef](#)]
30. Liu, Z.P.; Gao, Z.C.; Liu, Y.H.; Xia, M.S.; Wang, R.W.; Li, N. Heterogeneous Nanostructure Based on 1T-Phase MoS<sub>2</sub> for Enhanced Electrocatalytic Hydrogen Evolution. *ACS Appl. Mater. Interface* **2017**, *9*, 25291–25297. [[CrossRef](#)]
31. Yao, Y.; Ao, K.; Lv, P.; Wei, Q. MoS<sub>2</sub> Coexisting in 1T and 2H Phases Synthesized by Common Hydrothermal Method for Hydrogen Evolution Reaction. *Nanomaterials* **2019**, *9*, 844. [[CrossRef](#)] [[PubMed](#)]

**Disclaimer/Publisher's Note:** The statements, opinions and data contained in all publications are solely those of the individual author(s) and contributor(s) and not of MDPI and/or the editor(s). MDPI and/or the editor(s) disclaim responsibility for any injury to people or property resulting from any ideas, methods, instructions or products referred to in the content.